

and do not show any notable broadening in the presence of the microwave drive.

Magnons in a macroscopic-scale ferromagnetic crystal are now ready to be controlled in a quantum manner, enabling the investigation of the ultimate limit of spintronics and magnonics at the single-quantum level. It would be of particular interest to consider an analogy with recent advances in optoelectromechanics (26): Phonons in nanomechanical devices, yet another example of spatially extended collective excitations in solids, coherently interact both with microwave and optical degrees of freedom and thus are studied as a candidate for realizing quantum transducers between two spectrally distant frequency domains (27–29). Given the demonstrated strong coupling to microwave and the anticipated magneto-optical coupling, magnons in ferromagnetic insulators may provide an alternative route toward that goal.

REFERENCES AND NOTES

1. M. Sparks, *Ferromagnetic-Relaxation Theory* (McGraw-Hill, New York, 1964).
2. A. G. Gurevich, G. A. Melkov, *Magnetization Oscillations and Waves* (CRC Press, Boca Raton, FL, 2010).
3. S. O. Demokritov et al., *Nature* **443**, 430–433 (2006).
4. K. Uchida et al., *Nature* **455**, 778–781 (2008).
5. Y. Kajiwara et al., *Nature* **464**, 262–266 (2010).
6. H. Huebl et al., *Phys. Rev. Lett.* **111**, 127003 (2013).
7. Y. Tabuchi et al., *Phys. Rev. Lett.* **113**, 083603 (2014).
8. X. Zhang, C.-L. Zou, L. Jiang, H. X. Tang, *Phys. Rev. Lett.* **113**, 156401 (2014).
9. M. Goryachev et al., *Phys. Rev. Appl.* **2**, 054002 (2014).
10. K. Hammerer, A. S. Sørensen, E. S. Polzik, *Rev. Mod. Phys.* **82**, 1041–1093 (2010).
11. X. Zhu et al., *Nature* **478**, 221–224 (2011).
12. Y. Kubo et al., *Phys. Rev. Lett.* **107**, 220501 (2011).
13. J. J. Longdell, E. Fraval, M. J. Sellars, N. B. Manson, *Phys. Rev. Lett.* **95**, 063601 (2005).
14. S. Probst et al., *Phys. Rev. Lett.* **110**, 157001 (2013).
15. M. H. Devoret, R. J. Schoelkopf, *Science* **339**, 1169–1174 (2013).
16. R. Barends et al., *Nature* **508**, 500–503 (2014).
17. N. G. Dickson et al., *Nat. Commun.* **4**, 1903 (2013).
18. A. Wallraff et al., *Nature* **431**, 162–167 (2004).
19. O. Astafiev et al., *Science* **327**, 840–843 (2010).
20. M. Hofheinz et al., *Nature* **459**, 546–549 (2009).
21. Materials and methods are available as supplementary materials on Science Online.
22. A. Imamoglu, *Phys. Rev. Lett.* **102**, 083602 (2009).
23. P. J. Lee et al., *Phys. Rev. B* **79**, 180511 (2009).
24. E. Zakka-Bajjani et al., *Nat. Phys.* **7**, 599–603 (2011).
25. E. Flurin, N. Roch, J. D. Pillet, F. Mallet, B. Huard, *Phys. Rev. Lett.* **114**, 090503 (2015).
26. M. Aspelmeyer, T. J. Kippenberg, F. Marquardt, *Rev. Mod. Phys.* **86**, 1391–1452 (2014).
27. J. Bochmann, A. Vainsencher, D. D. Awschalom, A. N. Cleland, *Nat. Phys.* **9**, 712–716 (2013).
28. T. Bagci et al., *Nature* **507**, 81–85 (2014).
29. R. W. Andrews et al., *Nat. Phys.* **10**, 321–326 (2014).

ACKNOWLEDGMENTS

We acknowledge P.-M. Billangeon for fabricating the transmon qubit. This work was partly supported by the Project for Developing Innovation System of the Ministry of Education, Culture, Sports, Science and Technology, Japan Society for the Promotion of Science KAKENHI (grant no. 26600071, 26220601), the Murata Science Foundation, Research Foundation for Opto-Science and Technology, and National Institute of Information and Communications Technology (NICT).

SUPPLEMENTARY MATERIALS

www.sciencemag.org/content/349/6246/405/suppl/DC1
Materials and Methods
Figs. S1 to S4
References (30, 31)

25 November 2014; accepted 26 May 2015
Published online 9 July 2015;
10.1126/science.aaa3693

QUANTUM INFORMATION

Coherent coupling of a single spin to microwave cavity photons

J. J. Viennot,* M. C. Dartiailh, A. Cottet, T. Kontos*

Electron spins and photons are complementary quantum-mechanical objects that can be used to carry, manipulate, and transform quantum information. To combine these resources, it is desirable to achieve the coherent coupling of a single spin to photons stored in a superconducting resonator. Using a circuit design based on a nanoscale spin valve, we coherently hybridize the individual spin and charge states of a double quantum dot while preserving spin coherence. This scheme allows us to achieve spin-photon coupling up to the megahertz range at the single-spin level. The cooperativity is found to reach 2.3, and the spin coherence time is about 60 nanoseconds. We thereby demonstrate a mesoscopic device suitable for nondestructive spin readout and distant spin coupling.

The methods of cavity quantum electrodynamics hold promise for an efficient use of the spin degree of freedom in the context of quantum computation and simulation (1). Realizing a coherent coupling between a single spin and cavity photons could enable quantum nondemolition readout of a single spin, quantum spin manipulation, and facilitate the coupling of distant spins (1–4). It could also be used in hybrid architectures in which single spins are coupled to superconducting quantum bits (5), or to simulate one-dimensional spin chains (6).

The natural coupling of a spin to the magnetic part of the electromagnetic field is weak (7). To enhance it, one needs a large spin ensemble, typically of about 10^{12} spins (8–13), but these ensembles lose the intrinsic nonlinearity of a single spin 1/2. Alternatively, several theoretical proposals have been put forward to electrically couple single spins to superconducting resonators in a mesoscopic circuit (14–17), building on the exquisite accuracy with which superconducting circuits can be used to couple superconducting qubits and photons and manipulate them (18). One such approach is to engineer an artificial spin-photon interaction by using ferromagnetic reservoirs (15). Notably, the spin-photon coupling is also raising experimental efforts in the optical domain (19–23), but the circuit approach presents the important advantage of scalability.

Recent experiments have demonstrated the coupling of double quantum dot charge states to coplanar waveguide resonators, with a coupling strength $g_{\text{charge}} \approx 2\pi \times 10$ to 50 MHz (24–28). In (29), the spin blockade readout technique in quantum dots (30) was combined with charge sensing with a microwave resonator (31). In contrast to this spin-blockade scheme, here we use the ferromagnetic proximity effect in a coherent conductor to engineer a spin-photon coupling.

Our scheme relies on the use of a noncollinear spin-valve geometry, which realizes an artificial spin-orbit interaction (15). Specifically, we contact two noncollinear ferromagnets on a carbon nanotube double quantum dot.

Our device is shown in Fig. 1, A to C. Our resonator is similar to that used in a previous experiment (27), with a coupling scheme adapted from (24). It is a Nb resonator with a quality factor $Q \approx 6200$ to 11800, depending on the external magnetic field (see fig. S6). We use a previously developed technique of stamping to preserve the Q factor of the resonator and use nanotubes grown by chemical vapor deposition (32). The imprints of the stamps used to transfer the nanotubes are visible in Fig. 1A. We use PdNi as a ferromagnetic alloy. It forms good contacts with carbon nanotubes (33, 34), and its magnetization direction is simply controlled by the geometry of the electrodes (35). We set an angle (45° at zero magnetic field) between the magnetizations of the electrodes.

Ferromagnets deposited on carbon nanotubes induce effective magnetic fields (33, 36). In our setup, each dot is contacted to one ferromagnet, creating a local effective magnetic field and therefore a Zeeman splitting with a quantization axis given by the ferromagnet magnetization direction. When an electron is moved from one dot to the other, its equilibrium spin orientation rotates (Fig. 1D). As a consequence, we obtain an artificial spin-orbit coupling, engineered extrinsically. The localization of an electron wave function depends on the interdot energy detuning ϵ (31). This parameter is controlled experimentally with DC voltages applied with local top gates. Notably, because this control parameter is governed by electric fields, it is also actuated by the AC electric field associated with the photons in the resonator (24–29). A single electron spin is thus coupled to the photons of the resonator via the natural coupling of the double dots' charge orbitals to the resonator electric field (Fig. 1D). To tune the transition frequency of the spin states and bring them in resonance with the cavity frequency, we also apply an external magnetic field B_{ext} . The different contributions of real

Laboratoire Pierre Aigrain, Ecole Normale Supérieure–PSL Research University, CNRS, Université Pierre et Marie Curie–Sorbonne Universités, Université Paris Diderot–Sorbonne Paris Cité, 24 rue Lhomond, 75231 Paris Cedex 05, France.
*Corresponding author. E-mail: viennot@jila.colorado.edu (J.J.V.); kontos@ipa.ens.fr (T.K.)

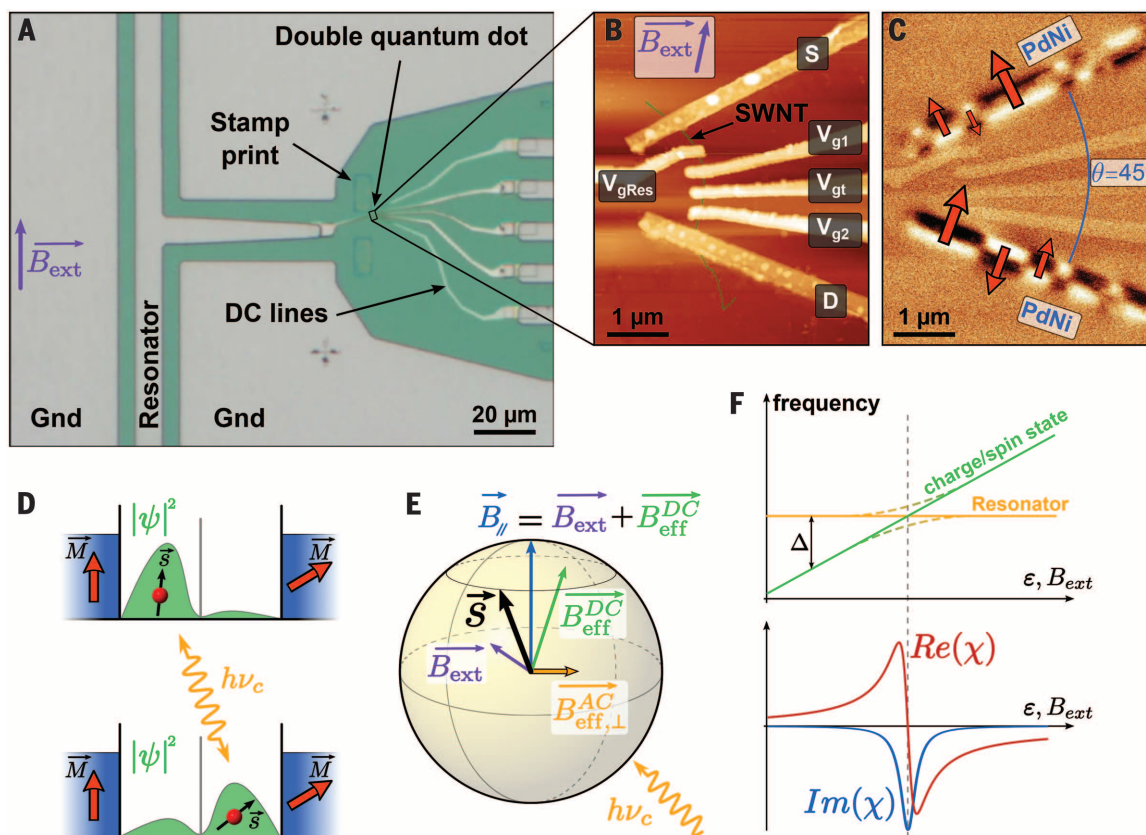
Fig. 1. Experimental setup.

(A) Optical micrograph of the essential part of the device. The resonator central conductor is surrounded by ground planes that are open in a small region, in order to place a carbon nanotube and the necessary DC lines to form a double quantum dot.

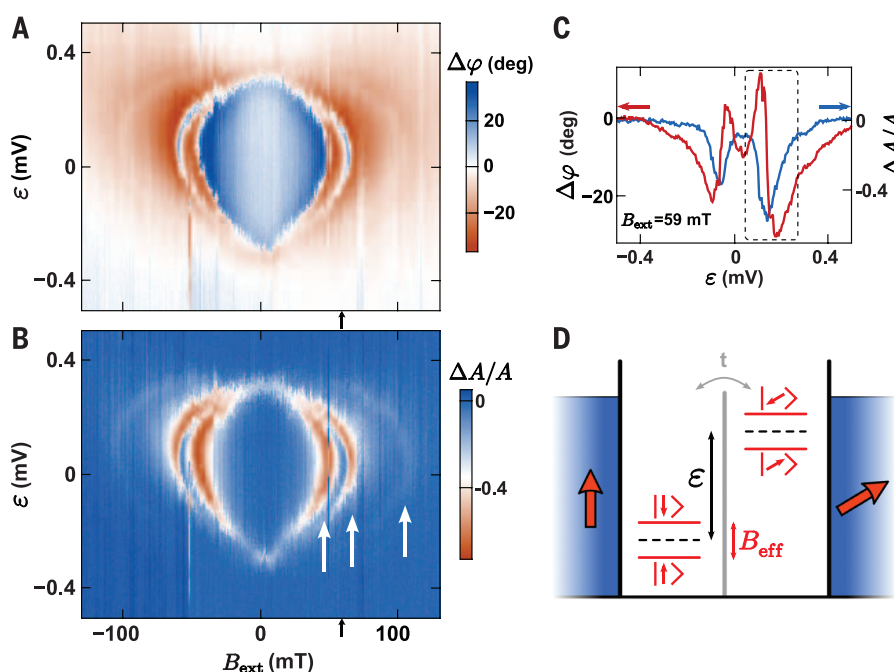
(B) Atomic force micrograph of the nanotube with four top gates used to bring DC electrical potentials, as well as couple to the resonator via V_{gRes} . As shown in the magnetic force micrograph **(C)**, source S and drain D electrodes are made out of a ferromagnetic alloy (PdNi). Black and white colors correspond to north and south poles of ferromagnetic domains.

(D) General principle of our coupling mechanism.

The proximity of the noncollinear ferromagnets induces a different equilibrium spin orientation if an electron is localized in the left or in the right dot. Photons are coupled to transitions changing the localization of the wave function Ψ and hence coupled to transitions changing the spin orientation. **(E)** Bloch sphere of the electron spin showing the different magnetic field contributions. **(F)** When a transition crosses—or anticrosses—the resonator frequency, the associated susceptibility exhibits a resonance that is directly observable in the phase and amplitude of the resonator transmission.

**Fig. 2. Electric and magnetic dependence of the quantum dot transitions.**

(A and B) Measured phase and amplitude signals as a function of external magnetic field and interdot gate detuning ϵ , at a microwave power $P \approx -116$ dBm (about 40 photons in the cavity). We identify three transitions (indicated by white arrows). The temperature is 40 mK. **(C)** Phase and amplitude versus ϵ at $B_{ext} = 59$ mT [indicated by black arrows in **(A)** and **(B)**], showing resonances similar to that in Fig. 1F within the dashed region. **(D)** Charge states (black dashed levels) are spin-split owing to the effective fields B_{eff} . The four states (red levels) coherently hybridize via the interdot tunnel coupling t .



and effective magnetic fields are depicted in Fig. 1E. The longitudinal component B_{\parallel} is given by the sum of the external magnetic field and the DC part of the effective fields, which depends on ϵ . This controls the Larmor frequency of the spin. When the electric field of the cavity actuates a charge modulation between the two dots, an AC effective magnetic field appears, with a transverse component $B_{\text{eff},\perp}^{\text{AC}}$ oscillating at the resonator frequency. This yields the two noncollinear magnetic fields necessary for transverse coupling to the spin: a DC longitudinal component, and a transverse AC component that can be oscillating at the Larmor frequency. Although the hybridization of the spin with the charge orbitals is the mechanism responsible for coupling to the electric field of the resonator, in principle this hybridization can be weak enough to preserve spin coherence (15). Moreover, the sensitivity to charge noise depends on the dispersion relation of the hybridized spin-charge transitions, and therefore it can have a behavior different from that of the spin-photon coupling strength. By sweeping ϵ , the resonant lines in Fig. 2, A and B, go through a “sweet spot” where the double quantum dot (DQD) transition frequencies are minimum and therefore insensitive to charge noise at first order. The existence of this sweet spot contributes to the high cooperativity found for the spin transitions.

We measure the amplitude A and phase ϕ of the cavity transmission at resonance, at 40 mK. We tune the gate voltages of the device to form a DQD (see fig. S1). Transitions in the DQD yield phase and amplitude shifts $\Delta\phi$ and $\Delta A/A$ of the resonator transmission. The intrinsic dependence of the superconducting cavity on the external magnetic field is taken into account in all measurements. For every change in B_{ext} the reference phase and amplitude are measured first, to obtain the correct $\Delta\phi$ and $\Delta A/A$ (37). A given transition between two DQD states $|i\rangle$ and $|j\rangle$ is characterized by a susceptibility to a microwave excitation $\chi_{ij} = \frac{g_{ij}}{-i\Gamma_{ij}/2 + \Delta_{ij}}$, where g_{ij} is the coupling

strength, Γ_{ij} is the decoherence rate, and Δ_{ij} is the frequency detuning (37). In practice, when such a transition is brought into resonance with the cavity mode, it shifts the mode frequency f_c by $\text{Re}(\chi_{ij})$ and changes the mode linewidth κ by $\text{Im}(\chi_{ij})$. The general form χ_{ij} is plotted in Fig. 1F. This signal is encoded in $\Delta\phi$ and $\Delta A/A$, which, to first order in χ_{ij} , are respectively given by $\text{Re}(\chi_{ij})$ and $\text{Im}(\chi_{ij})$. In the presence of multiple transitions, the phase and amplitude shifts are given by the sum of all the susceptibilities associated with transitions starting from a populated energy level (8, 24).

Figure 2, A and B, shows, respectively, the phase and amplitude shifts as functions of interdot gate detuning ϵ and external magnetic field B_{ext} . Sign changes are observed in $\Delta\phi$, together with dips in $\Delta A/A$, indicating DQD transition frequencies crossing the cavity frequency. Figure 2C shows a line cut at $B_{\text{ext}} = 59$ mT. The variation of the phase and amplitude in the dashed area of Fig. 2C resembles that in Fig. 1F.

Fig. 3. Spin-cavity hybridization.

(A) Measured transmission spectrum of the cavity as a function of B_{ext} , centered around the resonant frequency f_c , at small detuning $\epsilon \approx 50$ μ V. The temperature is 40 mK. (B) Resonator transmission at $B_{\text{ext}} = -67$ mT (indicated by the black arrow) with spin transition detuned ($\epsilon > 1$ mV, orange curve) and resonant ($\epsilon \approx 50$ μ V, green curve), measured at microwave power $P \approx -119$ dBm (about 20 photons in the cavity). Circles are data and solid line is theory [explained in (37)]. (C) Sketch of the spin transitions (Spin and Spin') dispersing with B_{ext} and hybridizing with the resonator mode (Cavity). Our measurements focus on the white stripe around the cavity frequency.

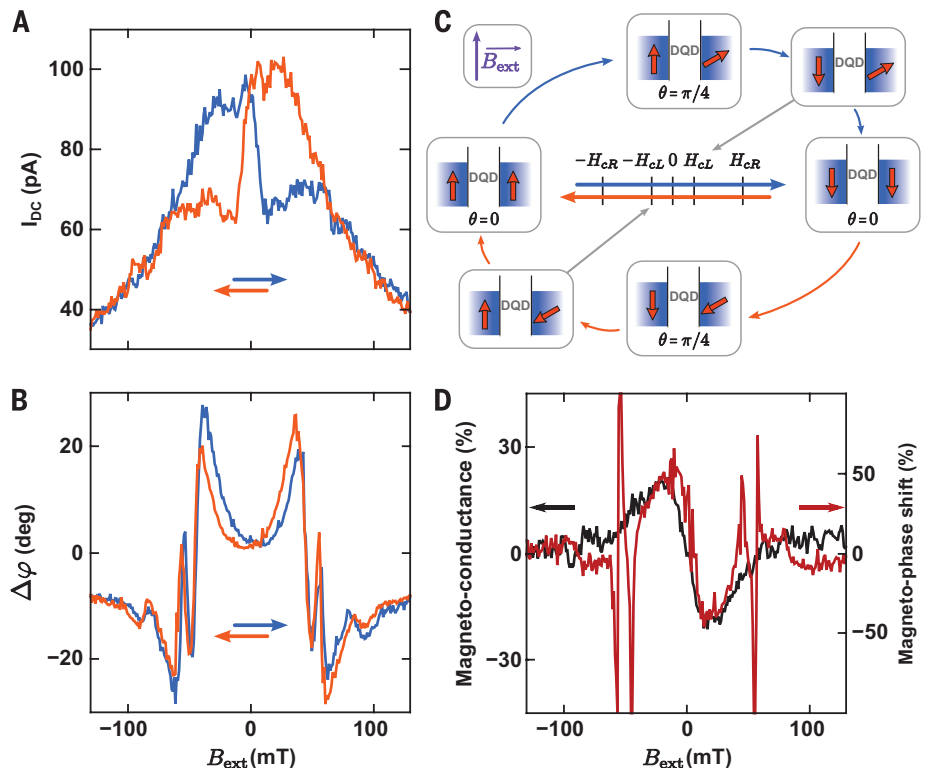
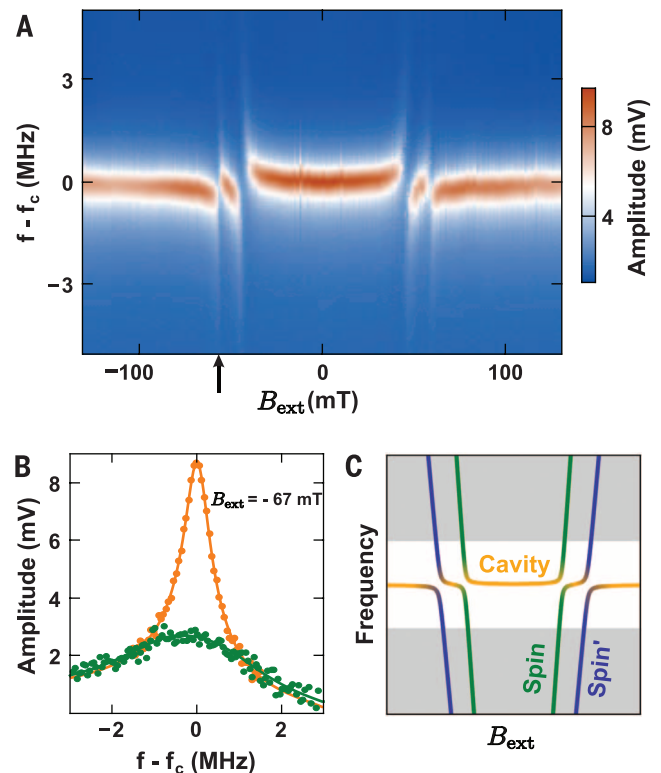


Fig. 4. Magnetic hysteresis. (A and B) Measured DC current and microwave phase shift for increasing (blue) and decreasing (orange) external magnetic field. See (37) for the details of the phase measurement. The temperature is 40 mK. (C) Schematics of the ferromagnets magnetization evolution with B_{ext} . H_{cL} and H_{cR} are the coercive fields of the ferromagnets. (D) Percentage of hysteresis for the DC current (magneto-conductance) and the phase signal (37).

Figure 2, A and B, therefore demonstrate that three transitions of the DQD are coupled to the cavity and disperse as functions of both ϵ and B_{ext} . This dependence on both gate voltage and magnetic field strongly suggests transitions involving changes in both charge and spin states (Fig. 2D). Charge states in the dots, separated by the energy ϵ , are Zeeman split by the effective fields induced by the ferromagnets. The tunnel coupling between the two dots coherently hybridizes their orbitals to form the analog of bonding and antibonding states (27, 31). In addition, the noncollinear quantization axis of the two dots couples the spin populations. The four states of Fig. 2D thus coherently hybridize into four quantum states having both charge and spin components.

When a transition is resonant with the cavity (i.e., around $\Delta_{ij} = 0$), the phase and amplitude contrasts are directly linked to the cooperativity:

$$C_{ij} = \frac{4g_{ij}^2}{\kappa\Gamma_{ij}}$$

The cavity linewidth κ varies slowly and by less than a factor of 2 in our magnetic field range ($2\pi \times 0.61$ MHz $< \kappa < 2\pi \times 1$ MHz; see fig. S6). Nevertheless, we observe a higher phase and amplitude contrast at higher fields and smaller interdot detuning ϵ (see Fig. 2, A and B). This indicates that transitions become more coherent, or more coherently coupled to the cavity in this region.

To perform a more quantitative analysis, we measure the resonator transmission spectrum as a function of the magnetic field at small interdot detuning ϵ of about 50 μ V (Fig. 3A). For the sake of clarity, the frequency traces are all centered around the bare cavity frequency f_0 , which itself shows jumps with changes in B_{ext} (see fig. S2 for the data in absolute frequency). At ± 50 mT, two DQD transitions become resonant with the cavity and cause strong distortions on the transmission spectrum. This confirms the high cooperativity between spin-hybridized transitions and the resonator. Figure 3B shows profiles of the resonator transmission at -67 mT, for a strongly detuned ($\epsilon > 1$ mV, orange curve) and a resonant transition ($\epsilon \approx 50$ μ V, green curve). We observe a pronounced change in the amplitude and width of the transmission. Fitting these data (37), we extract the bare cavity parameters and estimate the coupling strength $g_{\text{spin}} \approx 2\pi \times 1.3$ MHz for this transition, with a decoherence rate $\Gamma_{2,\text{spin}}^*/2 \approx 2\pi \times 2.5$ MHz, corresponding to a cooperativity $C \approx 2.3$ (37). We compare this to the much larger charge decoherence rate $\Gamma_{2,\text{charge}}^*/2 \approx 2\pi \times 0.45$ to 3 GHz measured previously in similar conditions on a carbon nanotube (27) and arising from charge noise. For the neighboring transition at -43 mT, we find that $C \approx 3.3$, which suggests that this transition is also dominantly a spin transition. Figure 3C shows a sketch of the spectrum obtained from a Hamiltonian generalized from (15) [see (37)]. In this sketch, we omit the third (faint) resonance visible in Fig. 2, A and B, because of its weaker coherence. The

calculated spectrum in (37) is in agreement with Fig. 3A. We are also able to reproduce the three resonances in Fig. 2, A and B (fig. S5). In our model, the two strongest resonances correspond dominantly to spin transitions, as expected. The third faint resonance corresponds to a transition that is less coherently coupled (37).

The final piece of evidence that the hybridized spin states arise from the extrinsic artificial spin-orbit interaction is provided by operating our device as a spin valve. To achieve that, we swept the magnetic field fast enough for the ferromagnetic electrodes to switch hysteretically. Figure 4A shows a conventional DC current measurement as a function of the magnetic field and the magnetic field sweeping direction, done on a cotunneling line (such as shown in fig. S1). We observe the characteristic hysteretic behavior of a quantum dot spin valve, which can be explained by the magnetization reversal sequence of Fig. 4C. This typically results in a magneto-conductance such as the one shown in Fig. 4D. Importantly, the electrodes' magnetizations are noncollinear, and one of them is not aligned with the magnetic field. The magnetization configuration is therefore noncollinear up to high enough B_{ext} , preserving the amplitude of spin-flipping matrix elements in the spin-photon Hamiltonian for transitions Spin and Spin' (15). Figure 4B shows the phase shift close to $\epsilon = 0$ for the same type of measurement as in Fig. 4A. The main part of the signal simply corresponds to the profile of Fig. 2A taken at small ϵ , showing the three transitions. Notably, the phase is hysteretic, revealing a hysteresis in the total susceptibility χ . We have ensured that this is not caused by spurious hysteresis of the cavity by measuring systematically all the cavity parameters along the hysteresis path (fig. S6). In Fig. 4D, we plot the hysteretic part of the phase shift (37). Sharp variations correspond to fields where the spin transition is resonant with the cavity. At these points, a small hysteresis in the transition frequency, therefore in the detuning Δ_{ij} , yields a strong hysteresis in the susceptibility. Outside of these areas, we observe a smooth variation similar to the behavior of the magneto-conductance. Both magneto-conductance and magneto-phase shift thus vary on the same scale of the magnetic field. This is further evidence that the spectrum is genuinely affected by the ferromagnets.

Along with a single spin-photon coupling strength $g_{\text{spin}} \approx 2\pi \times 1.3$ MHz, we can give a lower bound for the spin decoherence time in carbon nanotubes $T_2^* > 60$ ns ($T_2^* = 2/\Gamma_2^*$). This is already almost one order of magnitude larger than the previous measurements in nanotubes (38), but we believe that it could be improved further by optimizing the spin-charge hybridization. The cooperativity and decoherence rates given above indicate that our system is at the strong coupling threshold. Owing to the general principle used here, this method could be applied to many host materials for spin quantum bits. These results open an avenue for single spin-based circuit quantum electrodynamics experiments.

REFERENCES AND NOTES

1. A. Imamoglu et al., *Phys. Rev. Lett.* **83**, 4204–4207 (1999).
2. D. Loss, D. P. DiVincenzo, *Phys. Rev. A* **57**, 120–126 (1998).
3. G. Burkard, A. Imamoglu, *Phys. Rev. B* **74**, 041307 (2006).
4. J. M. Raimond, M. Brune, S. Haroche, *Rev. Mod. Phys.* **73**, 565–582 (2001).
5. D. D. Awschalom, L. C. Bassett, A. S. Zburak, E. L. Hu, J. R. Petta, *Science* **339**, 1174–1179 (2013).
6. I. Buluta, F. Nori, *Science* **326**, 108–111 (2009).
7. G. Tosi, F. A. Mohiyaddin, H. Huebl, A. Morello, *AIP Advances* **4**, 087122 (2014).
8. D. I. Schuster et al., *Phys. Rev. Lett.* **105**, 140501 (2010).
9. Y. Kubo et al., *Phys. Rev. Lett.* **105**, 140502 (2010).
10. H. Huebl et al., *Phys. Rev. Lett.* **111**, 127003 (2013).
11. Y. Tabuchi et al., *Phys. Rev. Lett.* **113**, 083603 (2014).
12. X. Zhu et al., *Nature* **478**, 221–224 (2011).
13. Y. Kubo et al., *Phys. Rev. Lett.* **107**, 220501 (2011).
14. M. Trif, V. N. Golovach, D. Loss, *Phys. Rev. B* **77**, 045434 (2008).
15. A. Cottet, T. Kontos, *Phys. Rev. Lett.* **105**, 160502 (2010).
16. P.-Q. Jin, M. Marthaler, A. Shnirman, G. Schön, *Phys. Rev. Lett.* **108**, 190506 (2012).
17. X. Hu, Y.-L. Liu, F. Nori, *Phys. Rev. B* **86**, 035314 (2012).
18. A. Wallraff et al., *Nature* **431**, 162–167 (2004).
19. W. B. Gao, P. Fallahi, E. Togan, J. Miguel-Sanchez, A. Imamoglu, *Nature* **491**, 426–430 (2012).
20. A. Faraon, C. Santori, Z. Huang, V. M. Acosta, R. G. Beausoleil, *Phys. Rev. Lett.* **109**, 033604 (2012).
21. E. Togan et al., *Nature* **466**, 730–734 (2010).
22. B. B. Buckley, G. D. Fuchs, L. C. Bassett, D. D. Awschalom, *Science* **330**, 1212–1215 (2010).
23. C. Arnold et al., *Nat. Commun.* **6**, 6236 (2015).
24. T. Frey et al., *Phys. Rev. Lett.* **108**, 046807 (2012).
25. H. Toida, T. Nakajima, S. Komiyama, *Phys. Rev. Lett.* **110**, 066802 (2013).
26. A. Wallraff, A. Stockklauser, T. Ihn, J. R. Petta, A. Blais, *Phys. Rev. Lett.* **111**, 249701 (2013).
27. J. J. Viennot, M. R. Delbecq, M. C. Dartailh, A. Cottet, T. Kontos, *Phys. Rev. B* **89**, 165404 (2014).
28. G.-W. Deng et al., Circuit QED with a graphene double quantum dot and a reflection-line resonator (2013); <http://arxiv.org/abs/1310.6118>.
29. K. D. Petersson et al., *Nature* **490**, 380–383 (2012).
30. K. Ono, D. G. Austing, Y. Tokura, S. Tarucha, *Science* **297**, 1313–1317 (2002).
31. R. Hanson, L. P. Kouwenhoven, J. R. Petta, S. Tarucha, L. M. K. Vandersypen, *Rev. Mod. Phys.* **79**, 1217–1265 (2007).
32. J. J. Viennot, J. Palomo, T. Kontos, *Appl. Phys. Lett.* **104**, 113108 (2014).
33. S. Sahoo et al., *Nat. Phys.* **1**, 99–102 (2005).
34. C. Feuillet-Palma et al., *Phys. Rev. B* **81**, 115414 (2010).
35. J.-Y. Chaudhary et al., *Phys. Rev. B* **84**, 094416 (2011).
36. J. R. Hauptmann, J. Paaske, P. E. Lindelof, *Nat. Phys.* **4**, 373–376 (2008).
37. Supplementary materials are available on Science Online.
38. E. A. Laird, F. Pei, L. P. Kouwenhoven, *Nat. Nanotechnol.* **8**, 565–568 (2013).

ACKNOWLEDGMENTS

We acknowledge fruitful discussions with the Quantronics group, J. M. Raimond, B. Huard, A. Thiaville, L. Bretheau, E. Flurin, L. E. Bruhat, and M. P. Desjardins and acknowledge the technical support of M. Rosticher and J. Palomo. We gratefully acknowledge P. Senellart and L. Lanco for discussions and for communicating results to us prior to publication. The work was financed by the European Union project SE2ND and the European Research Council Starting Grant CirQys. The data described in the paper are presented in this report and supplementary materials.

SUPPLEMENTARY MATERIALS

www.sciencemag.org/content/349/6246/408/suppl/DC1
Materials and Methods
Figs. S1 to S6

26 November 2014; accepted 29 June 2015
10.1126/science.aaa3786